

SURVEY FOR TRANSITING EXTRASOLAR PLANETS IN STELLAR SYSTEMS. I. FUNDAMENTAL PARAMETERS OF THE OPEN CLUSTER NGC 1245

CHRISTOPHER J. BURKE

Department of Astronomy, Ohio State University, 140 West 18th Avenue, Columbus, OH 43210; cjburke@astronomy.ohio-state.edu

B. SCOTT GAUDI

Harvard-Smithsonian Center for Astrophysics, 60 Garden Street, Cambridge, MA 02138; sgaudi@cfa.harvard.edu

AND

D. L. DEPOY, RICHARD W. POGGE, AND MARC H. PINSONNEAULT

Department of Astronomy, Ohio State University, 140 West 18th Avenue, Columbus, OH 43210; depoy@astronomy.ohio-state.edu, pogge@astronomy.ohio-state.edu, pinsono@astronomy.ohio-state.edu

Received 2003 December 3; accepted 2004 January 2

ABSTRACT

We derive fundamental parameters for the old, rich, open cluster NGC 1245 using *BVI* photometry from the MDM 1.3 m and 2.4 m telescopes. Based on detailed isochrone fitting, we find that NGC 1245 has a slightly subsolar metallicity, $[\text{Fe}/\text{H}] = -0.05 \pm 0.03$ (statistical) ± 0.08 (systematic) and an age of $1.04 \pm 0.02 \pm 0.09$ Gyr. In contrast to previous studies, we find no evidence of significant differential reddening. We determine an extinction of $A_V = 0.68 \pm 0.02 \pm 0.09$ mag and a distance modulus of $(m - M)_0 = 12.27 \pm 0.02 \pm 0.12$ mag, which corresponds to a distance of 2.8 ± 0.2 kpc. We derive a logarithmic mass function slope for the cluster of $\alpha = -3.12 \pm 0.27$, where a Salpeter slope is $\alpha = -1.35$. Fits to the radial surface density profile yield a core radius of $r_c = 3.10 \pm 0.52$ (2.57 ± 0.47 pc). NGC 1245 is highly relaxed and contains a strongly mass-segregated population. The mass function for the inner cluster has a very shallow slope, $\alpha = -0.56 \pm 0.28$. In contrast, the outer periphery of the cluster is enriched with low-mass members and devoid of high-mass members out to the tidal radius, $r_t = 20'$ (16.5 pc). Based on the observed surface density profile and an extrapolated mass function, we derive a total cluster mass, $M = 1300 \pm 90 \pm 170 M_\odot$.

Key words: open clusters and associations: individual (NGC 1245) — stars: fundamental parameters — stars: luminosity function, mass function

1. INTRODUCTION

Open clusters are excellent laboratories for many different aspects of astrophysics. First, open clusters form a coeval set of stars with homogeneous properties. This homogeneity makes it possible to determine with relative ease the age and metallicity of the cluster (Yi et al. 2001). Second, owing to their relatively small relaxation times, open clusters provide an opportunity to study stellar systems in various stages of dynamical evolution (Binney & Tremaine 1987). Finally, theory predicts that the star formation process within an open cluster is strongly affected by dynamical interactions, supernova explosions, and UV radiation (Adams & Myers 2001). Characterizing the fraction of cluster members with companions from stellar to planetary masses for a cluster in comparison with the field provides valuable insight into how these processes affect stellar and planetary formation.

The large angular size (tens of arcminutes to several degrees) of open clusters has traditionally made it difficult and time-consuming to observe a substantial fraction of an open cluster's members. However, recently available large-format CCD imagers now allow for complete studies of an open cluster with relatively small amounts of observing time. In this paper we present wide-field *BVI* photometry of the open cluster NGC 1245 using the MDM 8K Mosaic imager on the MDM 2.4 m Hiltner Telescope and supplemental *BVI* photometry obtained under photometric conditions on the MDM 1.3 m McGraw-Hill Telescope.

NGC 1245 is a rich, old open cluster with an approximately solar-metallicity population (Janes, Tilley, & Lyngå 1988; Wee & Lee 1996). The cluster is located toward the Galactic anticenter ($l = 147^\circ$, $b = -9^\circ$) at a distance $R \sim 2.5$ kpc (Janes et al. 1988; Wee & Lee 1996). With its relatively large Galactocentric distance, NGC 1245 is particularly useful in constraining the Galactic metallicity gradient (Friel 1995; Wee & Lee 1996). Here we improve on the observations for this cluster by covering a 6 times greater area, obtaining the first CCD *I*-band photometric data, and acquiring the first CCD data under photometric conditions. With these significant improvements over earlier studies, we are able to determine more precisely the physical parameters of the cluster as a whole, rather than just the inner cluster core. In addition to the observational improvements, we improve the interpretation of the observations by calculating the physical parameters of NGC 1245 using a χ^2 fit to the observations, and we make every effort to quantify the systematic errors in the derived physical parameters.

Because NGC 1245 is a rich open cluster and readily observable from our primary observing site, it is the first target of the Search for Transiting Extrasolar Planets in Stellar Systems (STEPSS) project (Burke et al. 2003). The goal of the STEPSS project is to assess the frequency of close-in extrasolar planets around main-sequence stars in several open clusters. Part of the *BVI* data we present in this paper were taken during a 19-night observing run to search for transiting extrasolar planets in NGC 1245. This transit data consist of

I-band-only observations obtained every 7 minutes with the MDM 8K Mosaic imager on the MDM 2.4 m telescope. Results of the search for extrasolar planets in NGC 1245 using this transit data will be presented in an upcoming paper (Gaudi et al. 2004). An additional paper presenting the variable star content of our NGC 1245 field based on light curves from the transit data is also in progress (Pepper et al. 2004). The main goal of this paper is to determine the fundamental physical parameters of NGC 1245. By determining the properties for this cluster and subsequent clusters in the STEPSS project, we will gain insight into how metallicity, age, and stellar density affect planetary formation, migration, and survival.

We describe our observations and data reduction in § 2. In § 3, we derive the physical parameters of NGC 1245 from isochrone fits to the *BVI* photometry. We derive the radial profile of NGC 1245 in § 4, the mass function in § 5, and the total mass in § 6. We present a summary and conclusions in § 7.

2. OBSERVATIONS AND DATA REDUCTION

2.1. Observations

We observed NGC 1245 on two occasions. The first set of observations was obtained in 2001 November using the MDM 8K mosaic imager on the MDM 2.4 m Hiltner Telescope. The MDM 8K imager consists of a 4×2 array of thinned 2048×4096 SITe ST002A CCDs (Crotts 2001). This instrumental setup yields a $26' \times 26'$ field of view and a $0''.36$ pixel⁻¹ resolution employing the 2×2 pixel binning mode. Table 1 shows, for each night of observations, the number of exposures in each filter, exposure time, median FWHM, and a brief comment on the observing conditions. This observing run is optimized for a transiting extrasolar planet search; thus, there are 960 *I*-band images obtained during this run that are not listed in Table 1. Since the emphasis of the present study is the color-magnitude diagram (CMD) of NGC 1245, from each night we chose only the *I*-band images that were taken concurrent with the other two filters and had the same number of images in order to have similar signal-to-noise characteristics for each filter. None of the nights was photometric. Therefore, we reobserved NGC 1245 in 2002 February using the MDM 1.3 m McGraw-Hill Telescope with the 2048×2048 “Echelle” imaging CCD. This CCD provides a $17' \times 17'$ field of view with $0''.5$ pixel⁻¹ resolution. Several nights were photometric, and we used Landolt (1992) standard star observations to

calibrate our photometry. Table 2 details the images taken with the MDM 1.3 m telescope. The relative placement between the 1.3 m and 2.4 m fields of view is shown in Figure 1.

Figure 1 shows a false-color image of NGC 1245 and shows the overlap between the MDM 2.4 m and 1.3 m data sets. The grid of eight numbered rectangles shows the field of view for the eight CCDs that make up the MDM 8K Mosaic imager. The large inscribed square is the field of view of the MDM 1.3 m observations. The blue, green, and red color channels for the false-color image result from a median combined image of the *B*, *V*, and *I* passbands, respectively. The circle denotes the cluster center derived in § 4.

2.2. Data Reduction

We use the IRAF¹ CCDPROC task for all CCD processing. We describe the 2.4 m data reduction first. The stability of the zero-second image over the course of the 19 nights allows us to median combine 95 images to determine a master zero-second calibration image. For master flat fields, we median-combined 11, 19, and 66 twilight sky flats taken throughout the observing run in the *B*, *V*, and *I* passbands, respectively. We quantified the errors in the master flat field by examining the night-to-night variability between individual flat fields. The small-scale, pixel-to-pixel variations in the master flat fields are $\sim 1\%$, and the large-scale, illumination-pattern variations reach the 3% level. The large illumination-pattern error resulted from a strong sensitivity in the illumination pattern to telescope focus. However, such large-scale variations do not affect photometry for which the point-spread function (PSF) scale is the most relevant.

We used the DAOPHOT package (Stetson 1987) within IRAF for PSF-fitting photometry, and we performed the photometry on each frame individually. To identify stars and to calculate stellar positions, we designate the highest signal-to-noise ratio *I*-band image as input to the DAOFIND task. We transformed the stellar positions determined on the high signal-to-noise *I*-band image to all the other images as initial guesses for photometry. To calculate the model PSF, we selected 25 bright, isolated stars evenly distributed on the reference image.

¹ IRAF is distributed by the National Optical Astronomy Observatory, which is operated by the Association of Universities for Research in Astronomy, Inc., under cooperative agreement with the National Science Foundation.

TABLE 1
MDM 2.4 m OBSERVATIONS

Date (2001)	Exposures	Filter	Exposure Time (s)	FWHM (arcsec)	Comments
Oct 27	9	<i>V</i>	300	1.4	Overcast
	9	<i>I</i>	300	1.1	
Nov 7	7	<i>V</i>	300	1.8	Partly cloudy
	7	<i>I</i>	300	1.2	
Nov 8	5	<i>B</i>	240	1.6	Cirrus
	5	<i>V</i>	240	1.5	
	5	<i>I</i>	240	1.3	
Nov 10	5	<i>B</i>	240	1.4	Cirrus
	5	<i>V</i>	240	1.6	
	5	<i>I</i>	240	1.3	
Nov 11	5	<i>B</i>	120	1.1	Clear
	5	<i>V</i>	120	1.1	
	5	<i>I</i>	120	1.0	
	1	<i>I</i>	240	0.9	

TABLE 2
MDM 1.3 m OBSERVATIONS

Date (2002)	Exposures	Filter	Exposure Time (s)	FWHM (arcsec)	Comments
Jan 31	2	<i>B</i>	120	2.0	Nonphotometric
	3	<i>V</i>	60	1.9	
	3	<i>I</i>	30	1.8	
	3	<i>I</i>	20	1.8	
Feb 5	6	<i>B</i>	120	1.7	Nonphotometric
	4	<i>V</i>	60	1.6	
	6	<i>I</i>	20	2.0	
Feb 7	2	<i>B</i>	90	1.6	Photometric
	2	<i>V</i>	60	1.4	
	3	<i>I</i>	20	1.7	

We used the same PSF stars for all images. Slight offsets between images result in at least 20 stars in the PSF model calculation for all the images. The PSF does not show any spatial variations. Modeling the spatially constant PSF model involves three iterations with faint neighbors to the PSF stars being subtracted from the image between iterations. Using the re-

sulting PSF model, the IRAF ALLSTAR task calculates the instrumental magnitudes by fitting the PSF model to all stars simultaneously. The reference image photometry defines our instrumental magnitude system, and we apply a zero-point offset to the individual image photometry to align them with the reference image photometry. A robust weighted mean using

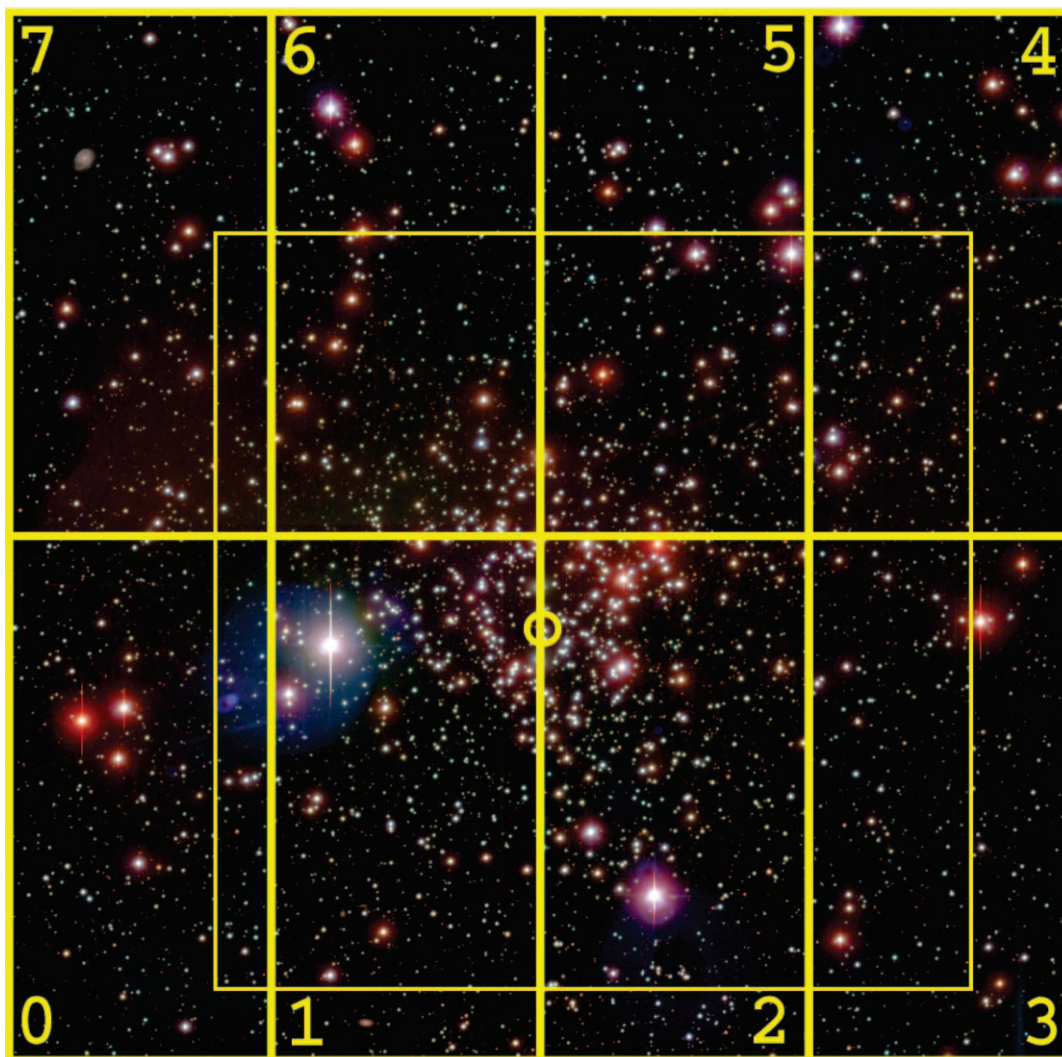


FIG. 1.—False-color image of the open cluster NGC 1245 obtained with the MDM 8K Mosaic imager (the 4×2 array of CCDs are numbered) on the MDM 2.4 m telescope. The large inscribed square is the field of view for the MDM 1.3 m telescope data obtained with a single CCD imager. The blue, green, and red color channels of the false-color image consist of combined images in the *B*, *V*, and *I* passbands, respectively. The circle shows the cluster center. North is to the right, and east is to the bottom.

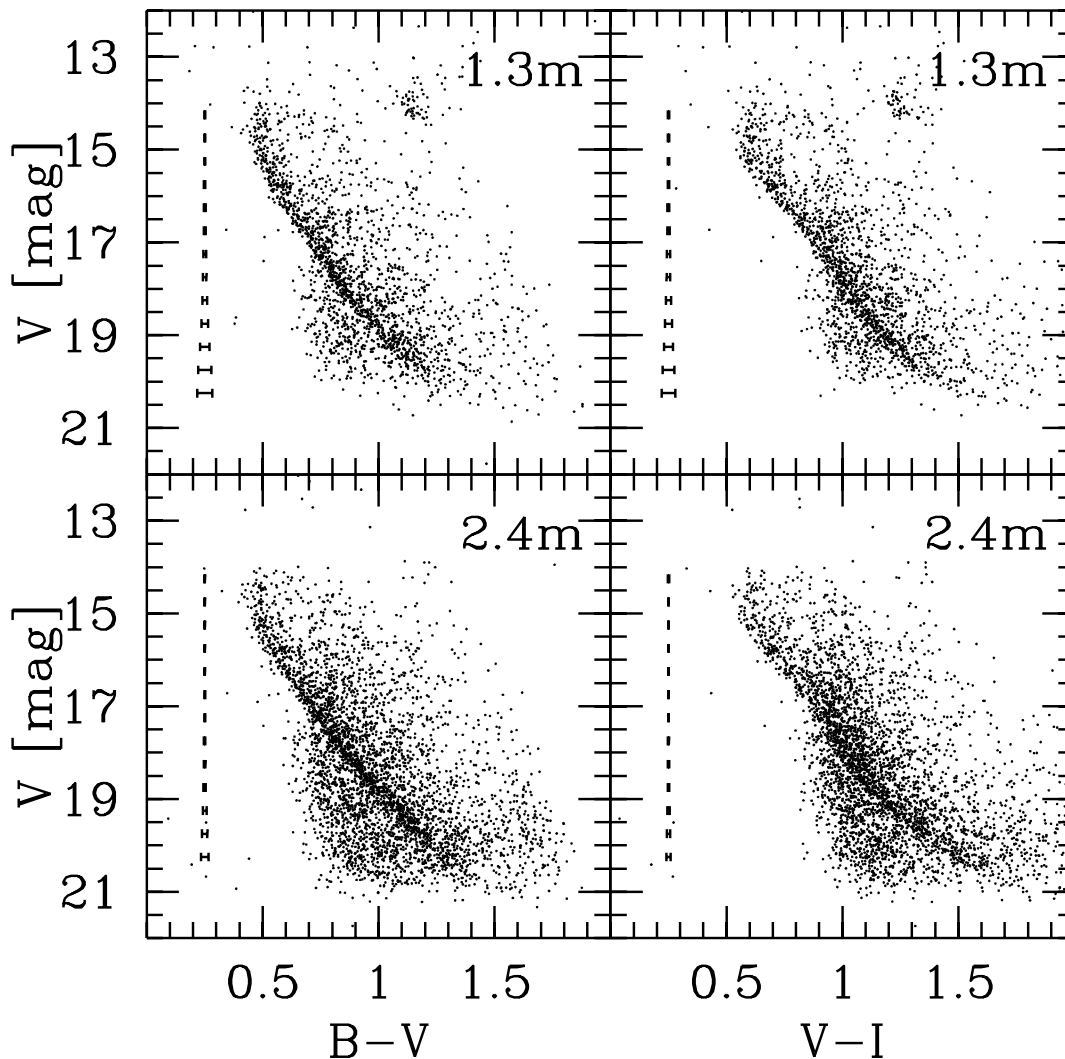


FIG. 2.—CMDs of the open cluster NGC 1245. Error bars represent the median sample standard deviation in the stellar color as a function of magnitude. *Top*: Data from the MDM 1.3 m telescope. *Bottom*: Data from the MDM 2.4 m telescope. *Left*: V vs. $B-V$. *Right*: V vs. $V-I$.

the errors output by ALLSTAR gives the final instrumental magnitude.

In order to place the MDM 2.4 m instrumental magnitudes onto a standard system, we used the IRAF FITPARAMS task to determine the transformation to the photometric MDM 1.3 m data set. The rms scatter for an individual star around the best-fit photometric transformation is ~ 0.03 mag in all passbands. This error represents how well an individual star approximates the photometric system defined by the 1.3 m data described below. The data taken with CCDs 1 and 3 of the MDM 8K mosaic imager suffered from a nonlinearity that reaches a level of 0.14 mag near full well. With the aid of the 1.3 m data set, this nonlinearity is correctable such that the errors in the photometric calibration for these CCDs are similar to the other CCDs not affected by the nonlinearity. The bottom panels of Figure 2 show the resulting CMDs for the MDM 2.4 m data set. The stars shown have sample standard deviations in the BVI photometry of less than 0.08 mag and at least three (B), three (V), and five (I) photometric measurements were returned from the photometry package without numerical convergence errors. The error bars in Figure 2 show the median of the sample standard deviations in the photometric color determination for stars in bins of

0.5 mag at V . These error bars represent the expected deviation from the mean of a color measurement from a single set of BVI exposures with signal-to-noise properties similar to our data set. Our ability to determine the mean color for a star requires dividing these errors by the \sqrt{N} of the number of measurements.

An alternative method to analyze the MDM 2.4 m data set is to combine the images and perform the photometry on this master combined image. The combined image enhances the signal-to-noise ratio of the faintest stars. This enhanced signal-to-noise ratio allows DAOFIND to detect and ALLSTAR to fit the model PSFs for significantly fainter stars at the expense of having to trust the error output from the photometry package. We median combine 15, 30, and 31 B , V , and I images, respectively, and perform the identical photometry procedure outlined above. Initial guesses for the stellar positions come from the combined I -band image. The instrumental magnitudes are fitted to the calibrated MDM 1.3 m data set with a simple zero point and color term. The resulting CMDs are shown in Figure 3. As one can see, these CMDs go significantly fainter, but the field star contamination becomes increasingly a problem, especially for the V , ($B-V$) CMD. The low contrast of the cluster's main sequence against the field

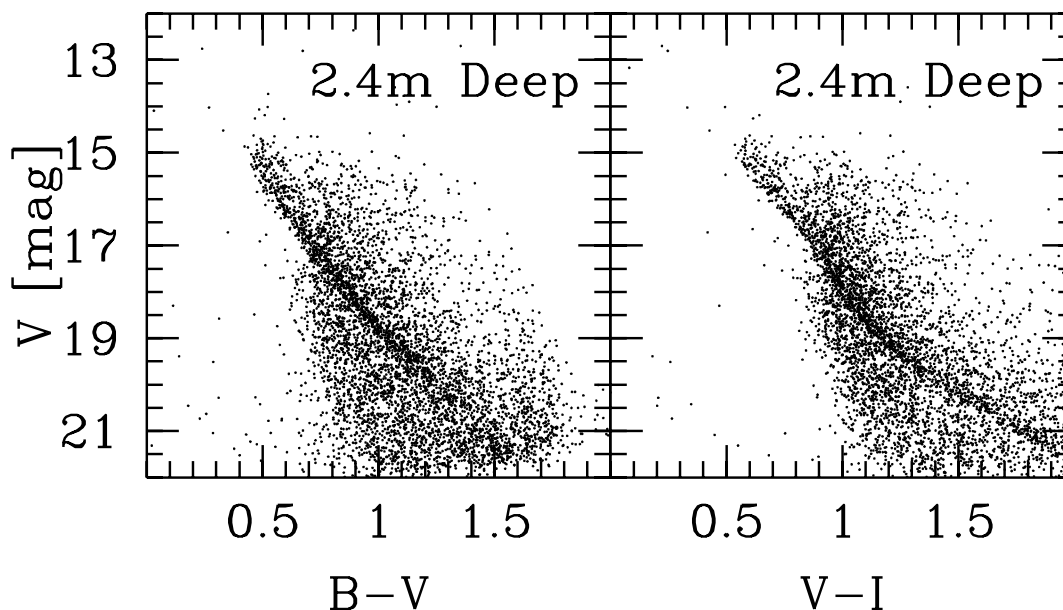


FIG. 3.—Deep CMDs of the open cluster NGC 1245 calculated by median combining the MDM 2.4 m data. *Left:* V vs. $B-V$. *Right:* V vs. $V-I$.

star contamination limits the utility of these deeper CMDs in determining the physical parameters of NGC 1245. In this study we only use these deep CMDs for extending our mass function toward fainter magnitudes (see § 5).

The analysis procedure for the MDM 1.3 m data set is similar to the MDM 2.4 m data set. The master zero-second image consists of a median combination of 49 images, and a master sky flat consists of a median combination of 12, 15, and 4 images for the B , V , and I passbands, respectively. The PSF has strong spatial variations, so we chose the same set of ~ 80 stars evenly distributed across a reference image to calculate a quadratically varying PSF model for each image individually. We employed the stand-alone ALLFRAME program (Stetson et al. 1998) to calculate the instrumental magnitudes for all images simultaneously. The aperture corrections are also spatially variable. We fit a third-order two-dimensional polynomial to the aperture corrections calculated on the evenly distributed PSF stars. The IRAF XYZTOIM task provides the best-fit solution for the two-dimensional polynomial aperture correction model. The standard deviation of the aperture correction is ~ 0.02 mag.

Aperture photometry measurements of the Landolt field SA101 (Landolt 1992) taken at three different air masses, $X = 1.2, 1.5,$ and 1.9 , on two separate photometric nights (see Table 2) provide a determination of the air-mass coefficient. The air-mass coefficients for the two nights are statistically identical; thus, we averaged both air-mass coefficient determinations for the final calibration. Fixing the air-mass coefficients, we calculated color terms for each night using observations of the Landolt fields G44-27, G163-50/51, and PG1407 (Landolt 1992). The color coefficients from the individual nights are also statistically identical, and we used the mean of both color coefficient determinations for the final calibration. The standard deviations in the calibrations are 0.015, 0.015, and 0.02 mag for the B , V , and I passbands, respectively. This represents how well an individual star approximates the photometric system outlined by Landolt (1992).

There are two, two, and three images in the B , V , and I passbands, respectively, of NGC 1245 that are photometric. After applying the aperture corrections to the ALLFRAME

instrumental magnitudes for the photometric data, we took a weighted mean of the measurements and then applied the photometric calibration to derive an initial standard star catalog. The final standard star catalog was obtained by applying the color term and aperture corrections to all nonphotometric MDM 1.3 m data, fitting for the zero-point offset to the initial standard star catalog, and calculating the robust weighted mean of all measurements.

In the process of determining the zero-point fit for the nonphotometric MDM 1.3 m data to the initial standard star catalog, we uncovered a 1.5% amplitude residual that correlates with spatial position on the CCD. The residual is negligible over most of the CCD, but the residual abruptly appears for stars with a position $x \lesssim 500$ in pixel coordinates. The residual linearly grows toward the decreasing x position on the detector reaching the 1.5% level at the edge. Because of the abrupt onset of this residual, even a cubically varying PSF model did not reduce the amplitude of the residual. To reduce the effect of this systematic spatial variability, we limited the zero-point fit for the nonphotometric MDM 1.3 m data to stars in the middle of the detector defined by $500 < x < 1500$ and $500 < y < 1500$ in pixel coordinates.

The top panels of Figure 2 show the resulting CMDs for the MDM 1.3 m data set. Only stars that have at least three photometric measurements returned from the photometry package without numerical convergence errors and a sample standard deviation < 0.08 mag in all three passbands are shown.

2.3. Comparison with Published Photometry

There is some confusion in the literature regarding the photometric calibration of NGC 1245. Carraro & Patat (1994) performed the first CCD detector study of NGC 1245. They calibrated their photometry by comparison with the photoelectric observations of Hoag et al. (1961). Unfortunately, the data of Carraro & Patat (1994), available on the widely used WEBDA open cluster database,² is incorrect, since it lacks the

² See <http://obswww.unige.ch/webda>.

photometric zero point as used in publication (G. Carraro 2003, private communication). Thus, using the incorrect data from WEBDA, Wee & Lee (1996) concluded the calibration of Carraro & Patat (1994) was incorrect. Our independent photometric calibration agrees with the earlier photoelectric studies. For five and three stars in common with the photoelectric studies of Hoag et al. (1961) and Jennens & Helfer (1975), respectively, we find V -band differences of 0.03 ± 0.06 and -0.012 ± 0.007 mag, respectively, and $B-V$ color differences of -0.01 ± 0.01 and -0.001 ± 0.02 mag, respectively. The $B-V$ colors of the stars used in the comparison span the range from 0.6 to 1.2 mag. Thus, the photometric calibration for NGC 1245 is well determined.

The recent study by Subramaniam (2003) does not find any differences with the Carraro & Patat (1994) photometry in the V band but does find a linear trend in the $B-V$ color difference as a function of V magnitude with an amplitude of 0.35 mag. It is unclear if the comparison with the Carraro & Patat (1994) photometry in Subramaniam (2003) is with the incorrect data from WEBDA. However, we do not find any $B-V$ color difference trends with the Carraro & Patat (1994) data. In addition, inspection of the Subramaniam (2003) CMD finds the giant clump is 0.35 mag redder in $B-V$ than in our CMD. The above comparisons call into question the Subramaniam (2003) color calibration.

3. PHYSICAL PARAMETERS

NGC 1245 is located in the Galactic plane ($b = -9^\circ$), and therefore, the observed field contains a large number of foreground and background disk stars complicating the process of fitting theoretical isochrones to the CMDs. We attempted to statistically subtract the field star population with a procedure similar to that of Mighell, Sarajedini, & French (1998). Unfortunately, because the contrast of the main sequence above the background field stars was relatively low (in comparison with the work by Mighell et al. 1998), we were unable to achieve a satisfactory background field subtraction.

Rather than statistically subtracting field contamination, we selected stars for the main-sequence isochrone fit by the following procedure. Since binaries and differential reddening affect the $B-V$ color of a star less than its $V-I$ color, the V , ($B-V$) CMD has a tighter main sequence than the V , ($V-I$) CMD. The tighter main sequence in the V , ($B-V$) CMD has a higher contrast above the contaminating field stars. Thus, to select main-sequence cluster members for the isochrone fit, we trace by eye the blue main-sequence edge in the V , ($B-V$) CMD. Shifting this trace redward by 0.12 mag defines the red edge selection boundary. Finally, shifting the trace 0.02 mag blueward defines the blue edge selection boundary. These shifts were selected by eye to contain a high fraction of the single-star main sequence. The vertical light solid lines in Figure 4 show the resulting main-sequence selection boundaries in the V , ($B-V$) CMD.

Since the difference in color between the red giant clump and the main-sequence turnoff in the CMD places strong constraints on the cluster age, we designate a box in the V , ($B-V$) CMD to select red giant members for the isochrone fit. The region with boundaries $13.7 < V < 14.4$ and $1.09 < (B-V) < 1.21$ defines the red giant clump selection. The light solid box around the red giant clump in the V , ($B-V$) CMD in Figure 4 shows the selection criteria for these stars. The red giant clump is saturated in the MDM 2.4 m data set, and therefore we fit isochrones to the MDM 1.3 m photometry only. There are 1004 stars that meet our main-sequence and red giant clump selection criteria.

For the isochrone fitting, we use the Yale-Yonsei (Y^2) isochrones (Yi et al. 2001), which employ the Lejeune, Cuisinier, & Buser (1998) color calibration. The Y^2 isochrones provide an interpolation scheme to calculate isochrones for an arbitrary age and metallicity within their grid of calculations. For a given set of isochrone parameters (metallicity, age, distance modulus, A_V , and R_V), we define the goodness of fit as

$$\chi_{\text{tot}}^2 = \sum_i \chi_i^2, \quad (1)$$

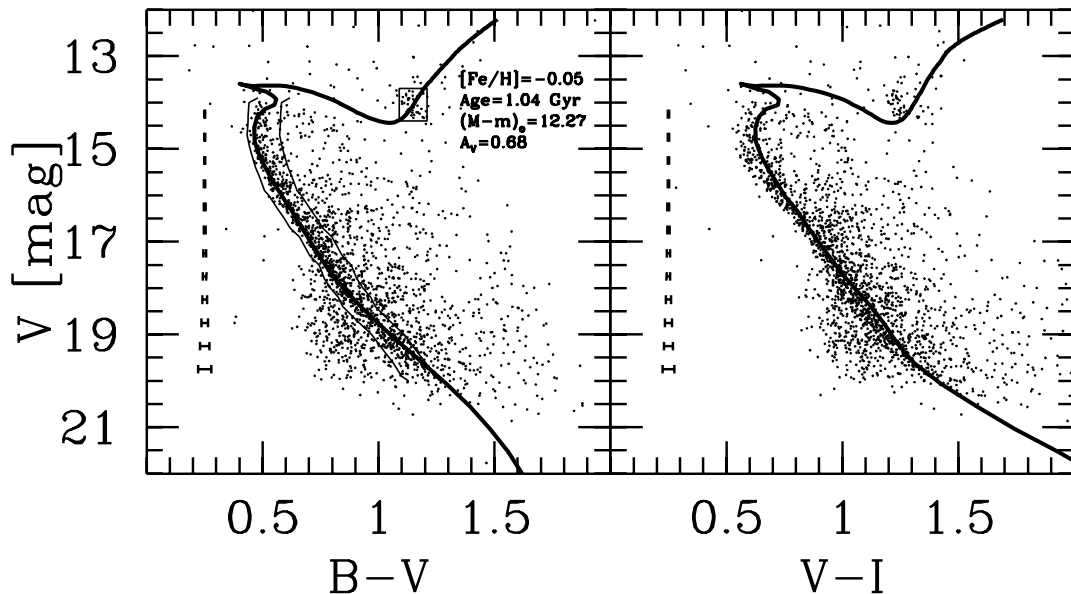


FIG. 4.—Best-fit isochrone solution (*heavy line*) overlying the color magnitude diagrams based on the MDM 1.3 m data. The light lines show the main-sequence and red giant clump selection boundaries.

where the sum is over all stars selected for isochrone fitting, and χ_i^2 is the contribution from star i ,

$$\chi_i^2 \equiv [B_{\text{pred}}(m_i) - B_{\text{obs},i}]^2 + [V_{\text{pred}}(m_i) - V_{\text{obs},i}]^2 + [I_{\text{pred}}(m_i) - I_{\text{obs},i}]^2. \quad (2)$$

In the preceding equation, BVI_{pred} are the magnitudes predicted by the isochrone, using the stellar mass, m_i , as the independent variable, and $BVI_{\text{obs},i}$ are the observed stellar magnitudes. We use the Brent minimization routine (Press et al. 2001) to determine the stellar mass that minimizes χ_i^2 for each star.

Theoretical isochrones and color calibrations contain systematic uncertainties that make it impossible to find a consistent fit to CMDs of the best studied open clusters over a wide range of colors and magnitudes (de Bruijne, Hoogerwerf, & de Zeeuw 2001; Grocholski & Sarajedini 2003). There are significant zero point and shape differences between published isochrones (Grocholski & Sarajedini 2003). A visual examination of the isochrone fits to observed CMDs in Grocholski & Sarajedini (2003) reveals that the systematic shape differences between published isochrones are most pronounced at the main-sequence turnoff and lowest observed masses. In order to avoid overemphasizing the main-sequence turnoff, where the photometric errors are the smallest and the systematic differences more pronounced, we adopt an equal weighting for all stars.

To find the best-fit isochrone parameters, we performed a grid search over age and metallicity. At fixed age and metallicity, we used the Powell multidimensional minimization routine (Press et al. 2001) to determine the best-fit distance modulus and reddening, A_V , by minimizing χ_{tot}^2 . To determine the reddening in the other passbands, A_B and A_I , we must assume a value for R_V , the ratio of total-to-selective extinction (Cardelli, Clayton, & Mathis 1989). For our best-fit solution, we fixed $R_V = 3.2$. We discuss the reasoning for this choice and its impact on the results in § 3.1. We calculated χ_{tot}^2 over a 40×40 evenly log-spaced grid of metallicity and age that ranges $-0.26 \leq [\text{Fe}/\text{H}] \leq 0.13$, and $0.7943 \text{ Gyr} \leq \text{age} \leq 1.4125 \text{ Gyr}$.

We determine our confidence limits on the model parameters by scaling the resulting χ^2 statistic,

$$\Delta\chi^2 = \frac{\chi_{\text{tot}}^2 - \chi_{\text{min}}^2}{\chi_{\text{min}}^2/\nu}, \quad (3)$$

where χ_{min}^2 is the minimum χ_{tot}^2 and ν is the number of degrees of freedom. Figure 5 is a contour plot showing the confidence region for the joint variation in metallicity and age. The three solid contours represent the 1, 2, and 3 σ confidence limits corresponding to $\Delta\chi^2 = 2.3, 6.14$, and 14.0 , respectively, for the 2 degrees of freedom. To further refine the best-fit isochrone parameters, we ran another 40×40 metallicity and age grid at a finer resolution: $-0.17 \leq [\text{Fe}/\text{H}] \leq 0.03$ and $0.9550 \text{ Gyr} \leq \text{age} \leq 1.2303 \text{ Gyr}$. We quantify the 1 σ error bounds by fitting a paraboloid to the $\Delta\chi^2$ surface as a function of the four fit parameters $[\text{Fe}/\text{H}]$, age, $(m - M)_0$, and A_V . The 1 σ errors are then the projection of the $\Delta\chi^2 = 1.0$ extent of this paraboloid on the parameter axes. We note that this procedure assumes that the $\Delta\chi^2$ surface near the minimum is parabolic, which we find to be a good approximation. Also, because we minimize on A_V and $(m - M)_0$ at fixed age and metallicity, we ignore the additional variance from these

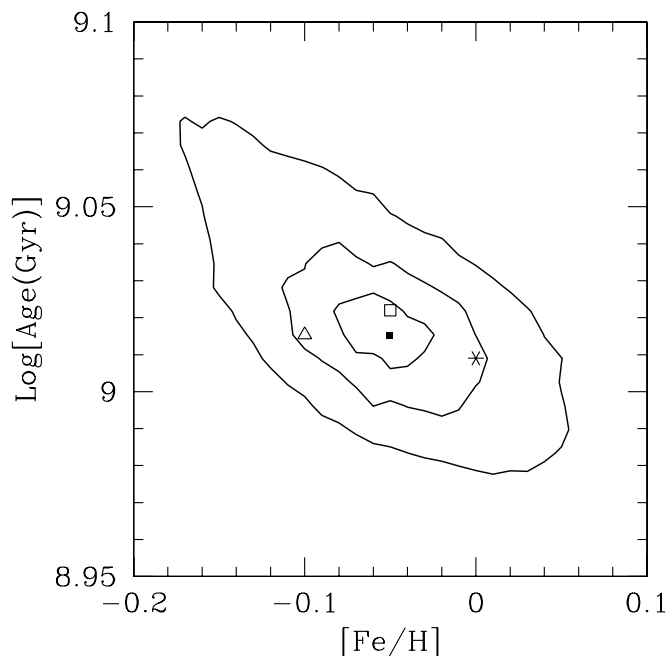


FIG. 5.—Contour lines represent the 1, 2, and 3 σ confidence regions on the joint variation in metallicity and age, showing the best-fit solution (filled square), the best-fit solution after reducing binary star contamination (open square), the best-fit solution assuming a ratio of selective-to-total extinction of $R_V = 3.0$ instead of $R_V = 3.2$ (triangle), and the best-fit solution assuming an I-band calibration fainter by 0.02 mag (asterisk).

parameters. Therefore, our errors are slightly underestimated. The resulting best-fit parameters are $[\text{Fe}/\text{H}] = -0.05 \pm 0.03$, age = $1.035 \pm 0.022 \text{ Gyr}$, $(m - M)_0 = 12.27 \pm 0.02 \text{ mag}$, and $A_V = 0.68 \pm 0.02 \text{ mag}$. The best-fit isochrone is overplotted on the V , $(B - V)$ and V , $(V - I)$ CMDs in Figure 4, and the best-fit metallicity and age are shown as the filled square in Figure 5.

The isochrone fits reasonably well in the V , $(B - V)$ CMD, deviating slightly too red toward the lower main sequence. We investigate whether an adjustment to the photometric calibration color term can reconcile the observed main sequence and the isochrone by first calculating the color residual between the stars and the isochrone at fixed V mag. A line fitted to the color residuals as a function of $B - V$ color has a slope $b = -0.065 \pm 0.007$. This calculation assumes that the V -band color term is correct, and only the B -band color term needs adjusting. The error in determining the color term, $1 \sigma \sim 0.004$ in all passbands, suggests the large, $b = -0.065$, color term adjustment required to reconcile the observed main sequence and theoretical isochrone does not result from an incorrect determination of the color term alone.

The fit is poorer in the V , $(V - I)$ CMD. Visually, the best-fit isochrone exhibits a tendency to lie redward of the main sequence in the V , $(V - I)$ CMD. This tendency toward the red partly results from the broader and more asymmetric main sequence in the V , $(V - I)$ CMD. In addition, the overly red isochrone results from systematic errors in the shape of the isochrone. The isochrone fits best near $V - I \sim 0.9$ and deviates redward of the main sequence toward fainter and brighter magnitudes. A line fit to the $V - I$ color residual between the stars and isochrone at fixed V mag as a function of $V - I$ color does not reveal any significant trend. Again, as with the V , $(B - V)$ CMD, the theoretical isochrones are unable to fit the detailed shape of the cluster main sequence from the turnoff

down to the lowest observed magnitudes. The isochrone deviates from the observed main sequence by as much as 0.06 mag in $V-I$ color at fixed V mag.

3.1. Systematic Errors

There are four main contributions to the systematic uncertainties in the derived cluster parameters: uncertainty in R_V , photometric calibration errors, theoretical isochrone errors, and binary star contamination. We address the effect of each of these uncertainties on the derived physical parameters in turn.

We can, in principle, determine R_V by additionally minimizing χ^2_{tot} with respect to R_V . However, in doing so we find a best-fit value of $R_V = 2.3$ and a metallicity of $[\text{Fe}/\text{H}] = -0.26$. Values of R_V this low are rare in our Galaxy (however, see Gould, Stutz, & Frogel 2001), and metallicity measurements based on medium resolution spectroscopic indices for NGC 1245 rule out a metallicity this low (Marshall et al. 2004).

We also can use infrared photometry from the 2MASS All Sky Data Release Point-Source Catalog (Cutri et al. 2003)³ to place more robust constraints on R_V . As a side note, 2MASS photometry does not reach nearly as faint as our BVI photometry. Thus, we do not include it directly in our best-fit solution for the physical parameters of NGC 1245. To aid in determining R_V , we constrain the sample of stars employed in the isochrone fit to stars with $V < 16$, which corresponds to $K_s \sim 14.5$ mag for turnoff stars. At this limiting magnitude, the typical photometric error in the 2MASS photometry is $\sigma_{K_s} \lesssim 0.07$. We transform the 2MASS K_s passband magnitudes to the K -band system defined by Bessell & Brett (1988; the system employed in the Lejeune et al. 1998 color calibration used by the Y^2 isochrones) by adding 0.04 mag to the 2MASS photometry (Cutri et al. 2003). The photometric transformation of the 2MASS photometry from K_s to K does not require a color term (Cutri et al. 2003). Using the $BVIK$ magnitudes of the $V < 16$ turnoff stars, we derive a best fit to the isochrones with $R_V \sim 3.2$. However, the resulting best-fit age is ~ 1.2 Gyr, somewhat older than the age of ~ 1.0 Gyr derived from the deeper BVI data alone. Conversely, fixing the age at ~ 1.0 Gyr in our isochrone fit to the turnoff stars, we find $R_V \sim 3.4$ is the best-fit solution. Figure 4 shows the best-fit isochrone to the BVI data systematically deviates from the observed main sequence at the turnoff. Since the 2MASS photometry limits our $BVIK$ isochrone fit to within 1.5 mag of the turnoff, we suspect the difficulty in determining R_V with an age consistent with our best-fit solution arises from systematic errors in the isochrones. We therefore adopt a fiducial value of $R_V = 3.2$ for our best isochrone fit but explore the impact a systematic uncertainty in R_V of 0.2 has on the cluster parameters in the following paragraph.

We quantify the effect of the systematic uncertainty in R_V on the cluster parameters by recalculating the isochrone fit assuming $R_V = 3.0$, the 1σ lower limit in our derived value of R_V . The resulting best fit is $[\text{Fe}/\text{H}] = -0.1$, age = 1.036 Gyr, $(m - M)_0 = 12.29$ mag, and $A_V = 0.68$ mag. The open triangle in Figure 5 shows the resulting best-fit metallicity and age for $R_V = 3.0$. Since the $B-V$ color is more sensitive to metallicity variations than the $V-I$ color, the color difference between the main sequence in the V_i ($B-V$) CMD and V_i ($V-I$) CMD is a good indicator of metallicity. Unfortunately, for a fixed A_V , variations in R_V also alter the relative $B-V$ and

$V-I$ color of the main sequence. This degeneracy between R_V and metallicity in determining the main-sequence color limits our ability to determine the metallicity.

To assess the systematic error associated with the photometric calibration uncertainty, we refitted the isochrones assuming the I -band photometry is fainter by 0.02 mag. The resulting best fit is $[\text{Fe}/\text{H}] = 0.0$, age = 1.021 Gyr, $(m - M)_0 = 12.31$, and $A_V = 0.62$. The I -band offset solution is shown as the asterisk point in Figure 5.

We attempt to investigate the systematic uncertainties in the isochrones by fitting the Padova group isochrones (Girardi et al. 2000) to the CMDs. We find that these isochrones do not match the shape of the observed main sequence. Systematic differences between the isochrones and data can reach up to 0.08 mag in $B-V$ and $V-I$ colors. The mismatch in shape to the observed main sequence prevents precise isochrone fits with the Padova isochrones, and we therefore cannot reliably quantify the systematic errors in the isochrones from these fits. However, we find that the solar-metallicity, 1 Gyr isochrone of the Padova group is broadly consistent with the observed data.

As an alternative method to quantify the systematic errors in the isochrones, we calculate the physical parameters for the well-studied Hyades open cluster using a procedure identical to that used for the NGC 1245 data. The Hyades CMD data are selected for membership based on proper motion and are cleaned of binary star contaminants based on spectroscopic observations (see Pinsonneault et al. 2003 for a discussion of the data and membership selection). Using a metallicity and age grid with resolution $\Delta[\text{Fe}/\text{H}] = 0.01$ dex and $\Delta \log(\text{age}) = 0.006$ dex, we find best-fit isochrone parameters of $[\text{Fe}/\text{H}] = 0.10$, age = 670 Myr, $(m - M)_0 = 3.23$ mag, and $A_V = 0.03$ mag. The recent study by Paulson, Sneden, & Cochran (2003) and many previous studies determine a value of $[\text{Fe}/\text{H}] = 0.13 \pm 0.01$ for the metallicity of the Hyades using high-resolution spectroscopy. Perryman et al. (1998) find an age of 625 ± 50 Myr using an independent set of isochrones. The *Hipparcos* distance to the Hyades is $(m - M)_0 = 3.33 \pm 0.01$ mag (Perryman et al. 1998), and the extinction for the Hyades is commonly cited as negligible. The difference in the physical parameters of the Hyades from our isochrone fit to the more accurate determinations of these parameters provides the relative systematic error in our isochrone fitting technique due to systematic errors in the isochrones.

The final systematic error source we address is the error resulting from contamination due to unresolved binaries. Unresolved binaries tend to lie redward of the single-star main sequence, and this binary “reddening” has a larger effect on the $V-I$ color than on the $B-V$ color. Thus, the main sequence in a V_i ($V-I$) CMD is not as tight and shows greater intrinsic scatter than the V_i ($B-V$) CMD because the unresolved binaries are separated in $V-I$ color from the single-star main sequence more than they are in $B-V$ color. An additional selection of the main sequence in the V_i ($V-I$) CMD provides a sample of probable cluster members with reduced contamination by unresolved binaries. For determining the additional main-sequence selection in the V_i ($V-I$) CMD, we trace by eye the blue boundary of the main sequence. The red main-sequence boundary is defined by offsetting the blue boundary by 0.08 mag in color. A 0.15 mag color offset is needed to select most of the stars that meet the original main-sequence selection based on the V_i ($B-V$) CMD alone. This additional main-sequence selection reduces the stellar sample to 584 from the original 1004. The best-fit isochrone using stars that

³ See <http://www.ipac.caltech.edu/2mass/releases/allsky/doc/explsup.html>.

meet the main-sequence selection criteria in both CMDs has parameters $[\text{Fe}/\text{H}] = -0.05$, age = 1.052 Gyr, $(m - M)_0 = 12.33$ mag, and $A_V = 0.62$ mag. The above solution is shown as the empty square in Figure 5.

To define the 1σ systematic error on the fitted parameters, we use the difference between the best-fit parameters and the parameters determined during the above discussion of the three sources of systematic error: uncertainty in R_V , photometric calibration, and binary star contamination. For the 1σ systematic error in the theoretical isochrones, we use the relative difference between our isochrone fit parameters for the Hyades and the quoted values from the literature. To derive an overall systematic error in the cluster parameters, these four sources of systematic error are added in quadrature. The resulting overall 1σ systematic errors are $\sigma_{[\text{Fe}/\text{H}]} = 0.08$, $\sigma_{\text{age}} = 0.09$ Gyr, $\sigma_{(m-M)_0} = 0.12$ mag, and $\sigma_{A_V} = 0.09$ mag. The photometric calibration and R_V uncertainty dominate the systematic uncertainty in metallicity. The systematic uncertainty in the isochrone dominates the systematic uncertainties in the age and distance. Unresolved binary contamination and photometric calibration dominate the uncertainty in the reddening.

3.2. Comparison with Other Determinations

The best-fit metallicity we derive from isochrone fitting to NGC 1245 agrees with our independent metallicity determination using spectroscopy of individual red giant members (Marshall et al. 2004). Medium-resolution spectroscopic indices calibrated from high-resolution spectroscopy indicate $[\text{Fe}/\text{H}] = -0.06 \pm 0.12$, where the error is the 1σ systematic error in the spectral index–metallicity calibration. Wee & Lee (1996) measure the metallicity of NGC 1245 using Washington photometry and obtain $[\text{Fe}/\text{H}] = -0.04 \pm_{\text{stat}} 0.05 \pm_{\text{syst}} 0.16$. We note that NGC 1245 is commonly quoted in the literature as having a supersolar metallicity of $[\text{Fe}/\text{H}] = +0.14$ as given by the Lyngå (1987) open cluster database.⁴ The origin of this high metallicity for NGC 1245 is unclear; the source for the high metallicity as given in Lyngå (1987) does not contain observations for or even discuss NGC 1245.

Our best-fit age for NGC 1245 is in agreement with the age of 1.1 ± 0.1 Gyr found by Wee & Lee (1996). Carraro & Patat (1994) and Subramaniam (2003) find a younger age of 800 Myr for NGC 1245. In the case of Carraro & Patat (1994), the younger age most likely results from their assumption of $[\text{Fe}/\text{H}] = +0.14$ for the cluster. In the case of Subramaniam (2003), the difference in color between the main-sequence turnoff and the red giant clump requires the younger age. We believe the red giant clump of Subramaniam (2003) is too red by 0.35 mag in $B-V$ color (as discussed in § 2). Our smaller color difference between the main-sequence turnoff and the red giant clump results in the older age for NGC 1245.

The main differences between this study and previous investigations of NGC 1245 are that we find a lower overall reddening and no evidence for significant differential reddening. We find $E(B-V) = 0.21 \pm 0.03$, where the error includes the systematic uncertainty in R_V and A_V . Previous studies find higher reddenings $E(B-V) = 0.28 \pm 0.03$ (Wee & Lee 1996), marginally consistent with our determination. The previous claims for differential reddening across NGC 1245 have not been highly significant and even conflicting.

Carraro & Patat (1994) determine a north-south $B-V$ color gradient of 0.04 mag arcmin⁻¹ with redder colors toward the south, and (Wee & Lee 1996) find a north-south $B-V$ color gradient of 0.03 ± 0.16 mag arcmin⁻¹, except the color gradient is in the opposite sense, with redder colors to the north.

We follow the same procedure as Carraro & Patat (1994) and Wee & Lee (1996) to determine the differential reddening across NGC 1245 using the 1.3 m data set. To quantify the differential reddening across NGC 1245, we start with the same sample of stars that were used for the isochrone fit. We further restrict the sample to stars with $15.0 \leq V \leq 17.0$ mag. The differential reddening is modeled as a linear trend between the $B-V$ color of stars as a function of north-south position. We formally find a north-south $B-V$ color gradient of 0.0042 ± 0.0006 mag arcmin⁻¹ with redder colors to the north. The color gradient corresponds to a total change of $\Delta(B-V) \sim 0.03$ over $9'$. The color gradient in the east-west direction is half the north-south color gradient with a similar error. Therefore, we find a color gradient that is smaller by an order of magnitude than previous investigations. Furthermore, although formally significant, we are not convinced of the color gradient's reality because the two-dimensional aperture correction map and PSF variations both contain errors of order 0.02 mag.

4. RADIAL PROFILE

Stellar encounters drive an open cluster toward equipartition of kinetic energy resulting in mass segregation of the cluster members (Binney & Tremaine 1987). The survey of Nilakshi et al. (2002) demonstrates that the prominent cores of open clusters generally contain the most massive stars, but 75% of a cluster's mass lies in a surrounding corona containing only low-mass members of the cluster. In this section, we search for the signatures of mass segregation in NGC 1245 by studying its radial surface density profile as a function of the magnitude of the cluster stars.

The first step in deriving the radial profile is to locate the cluster center. Using the stellar positions for stars with high-quality photometry shown in the 1.3 m CMD (Fig. 2), we spatially smoothed the number counts with a Gaussian of radius $\sim 75''$. We did not use the 2.4 m data set to calculate the cluster center because gaps in the CCD array bias the derived center. The open circle in Figure 1 denotes the cluster center. Our derived cluster center is located $48''$ east and $75''$ south of the center determined by Carraro & Patat (1994) and $36''$ east and $36''$ south of the center determined by Subramaniam (2003). Since neither study gives exact details on how the cluster center was determined, we cannot determine the significance of these differences in the cluster center. However, we believe that our estimate for the cluster center is likely to be more robust, because of our larger field of view and fainter limiting magnitude.

We constructed a radial surface density profile by determining the surface density of stars in concentric annuli of width $\sim 25''$. The top left panel in Figure 6 shows the surface density profile derived from both the 1.3 and 2.4 m data sets. We approximate the errors as $N_i^{1/2}$, where N_i is the number of stars in each bin. Area incompleteness sets in because of the finite size of the detector for annuli $\geq 7/3$ in the 1.3 m data set and $\geq 11/6$ for the 2.4 m data set, thereby increasing the errors. Generally, the surface density profiles derived from the two data sets agree well, except near the center of the cluster and a small overall scaling. The scaling difference results from the

⁴ See <http://vizier.u-strasbg.fr>.

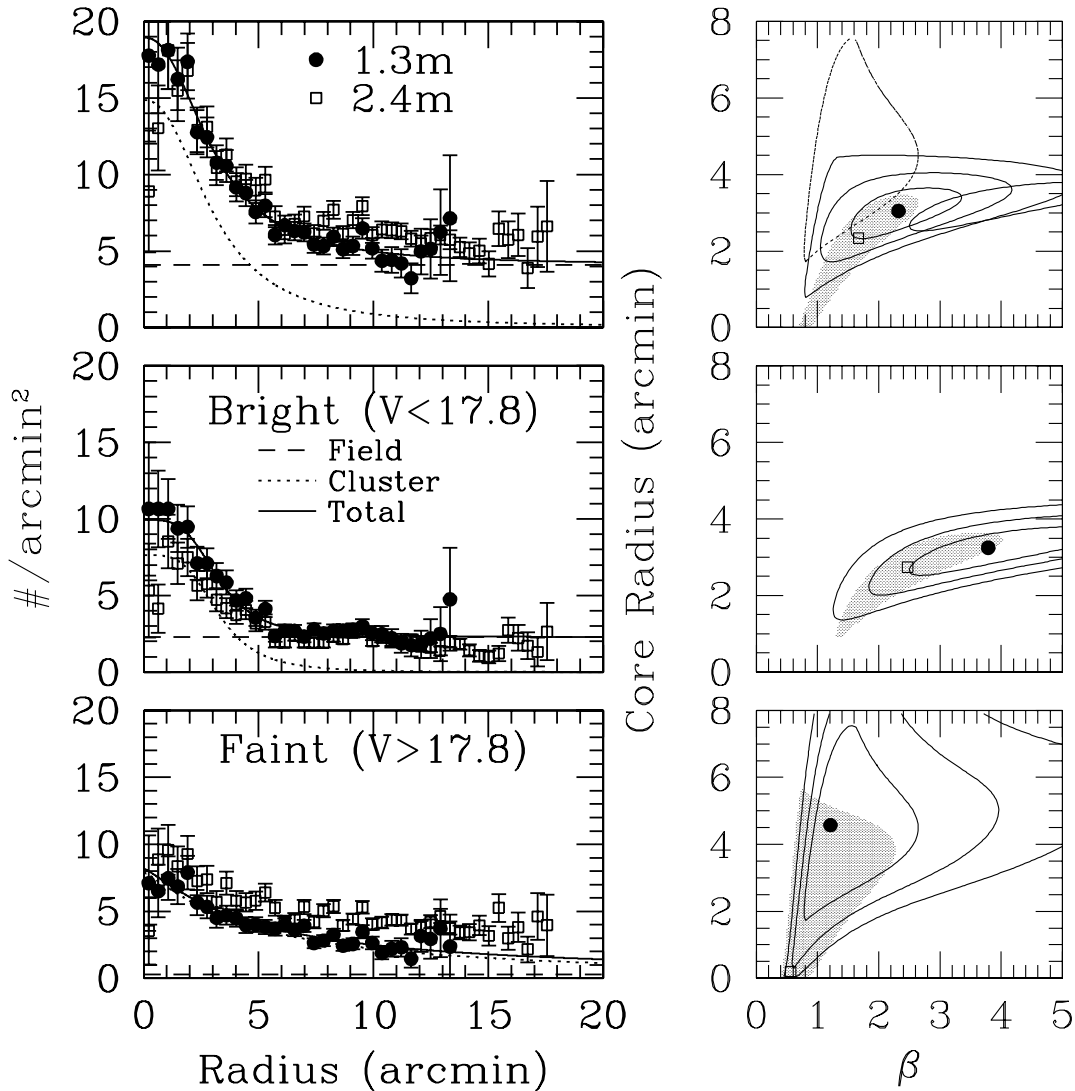


FIG. 6.—*Left*: Radial surface density profiles of stars in the NGC 1245 field for three different samples of stars. *Top*: Radial profile for all stars. *Middle*: Profile for the subset of these stars with $V < 17.8$. *Bottom*: Profile for stars with $V > 17.8$. The circles are derived from the 1.3 m data, while the squares are from the 2.4 m data. In each panel, the solid line shows the best-fit model to the 1.3 m data, which is composed of a cluster profile (*dotted line*) plus a constant field star surface density (*dashed line*). *Right*: The 68%, 95%, and 99% confidence regions on the fitted logarithmic slope of the density profile β and core radius for the 1.3 m data. The circle shows the best-fit model for the 1.3 m data, whereas the square is the best fit for the 2.4 m data set. The shaded region is the 68% confidence region for the fit to the 2.4 m data set. In the top right panel, we also show the 68% confidence regions for the bright and faint samples.

fainter limiting magnitude in the 2.4 m data set (see Fig. 2). The discrepancy in the inner annuli arises from the fact that the cluster center falls very close to a gap in the CCD array for the 2.4 m detector. Therefore, incompleteness affects the first few radial bins of the 2.4 m surface density profile. We disregard the first two radial bins for all surface density profiles derived from the 2.4 m data set.

As expected, the radial profile of the cluster exhibits a gradual decline to a constant field star surface density. We fit the surface density profile to the model,

$$\Sigma(r) = \Sigma_f + \Sigma_0 \left[1 + \left(\frac{r}{r_c} \right)^\beta \right]^{-1}, \quad (4)$$

where Σ_f is the surface density of field stars, Σ_0 is the cluster surface density at $r = 0$, and r_c is the core radius. In fitting equation (4), we require a positive Σ_f . We fit this profile to both the 1.3 and 2.4 m data sets. Although the 2.4 m surface

density profile extends to larger radii, the incompleteness near the center generally results in less well-constrained parameters, in particular the core radius r_c .

Both fits are excellent: for the 1.3 m data set, $\chi^2 = 15.9$ for 28 degrees of freedom (dof), whereas for the 2.4 m data set, $\chi^2 = 39.3$ for 36 dof. Table 3 tabulates the best-fit parameter values and 1σ uncertainties for all data sets. A parabola fitted to the envelope of χ^2 values as a function of the parameter of interest determines the parameter's error. The solid line in the top left panel of Figure 6 shows the best-fit model to the 1.3 m profile. The logarithmic slope of the surface density is $\beta = 2.36 \pm 0.71$, and the core radius is $3'.10 \pm 0'.52$. The field and central surface densities are $\Sigma_f = 4.0 \pm 0.8 \text{ arcmin}^{-2}$ and $\Sigma_0 = 14.7 \pm 2.9 \text{ arcmin}^{-2}$, respectively. At the derived distance to the cluster, $d = 2850 \text{ pc}$, the conversion from angular to physical distances is $1'.207 \text{ pc}^{-1}$. Thus, NGC 1245 has a core radius of $\sim 2.6 \text{ pc}$. The core radius agrees with the previous determination of $2'.7 \pm 0'.13$ from Nilakshi et al. (2002).

TABLE 3
 FITTED PARAMETERS AND 1σ ERRORS TO SURFACE DENSITY PROFILES

Data Set	Sample	Σ_f^a (arcmin ⁻²)	Σ_0^a (arcmin ⁻²)	r_c^b (arcmin)	β	Σ_f^a (model) (arcmin ⁻²)
1.3 m.....	All	4.05 ± 0.84 (5.90 ± 1.22)	14.72 ± 2.88 (21.43 ± 4.20)	3.10 ± 0.52 (2.57 ± 0.43)	2.36 ± 0.71	5.087 ± 0.040 (7.401 ± 0.058)
	Bright	2.29 ± 0.23 (3.33 ± 0.34)	7.61 ± 1.52 (11.08 ± 2.21)	3.27 ± 0.51 (2.72 ± 0.42)	3.87 ± 1.34	2.189 ± 0.024 (3.187 ± 0.035)
	Faint	0.49 ± 1.93 (0.71 ± 2.80)	7.76 ± 3.47 (11.29 ± 5.05)	4.61 ± 2.42 (3.82 ± 2.00)	1.29 ± 0.88	2.887 ± 0.028 (4.203 ± 0.041)
2.4 m.....	All	4.70 ± 1.10 (6.84 ± 1.61)	18.89 ± 12.19 (27.51 ± 17.8)	2.22 ± 1.44 (1.84 ± 1.19)	1.66 ± 0.78	5.440 ± 0.039 (7.920 ± 0.057)
	Bright	1.59 ± 0.28 (2.32 ± 0.40)	7.58 ± 3.03 (11.04 ± 4.41)	2.75 ± 0.95 (2.28 ± 0.79)	2.53 ± 1.06	2.053 ± 0.025 (2.989 ± 0.036)
	Faint	1.54 ± 3.14 (2.24 ± 4.57)	29.17 ± 43.21 (42.46 ± 62.91)	0.40 ± 5.01 (0.33 ± 4.15)	0.70 ± 1.29	3.379 ± 0.030 (4.919 ± 0.044)

^a Values in parentheses are in units of pc⁻².

^b Values in parentheses are in units of parsecs.

To investigate mass segregation, we next divide the high-quality–photometry sample of stars into two subsamples: bright stars with $V < 17.8$ and faint stars with $V > 17.8$. There are roughly an equal number of cluster stars in each subsample. The surface density profiles for both the 1.3 m and 2.4 m data are shown in the bottom left and middle left panels of Figure 6. We find a significant difference between the best-fit logarithmic slopes of the bright and faint subsamples. For the 1.3 m data set, we find $\beta = 3.9 \pm 1.3$ for the bright sample and $\beta = 1.3 \pm 0.9$ for the faint sample. This provides evidence, at the $\sim 2 \sigma$ level, that the faint cluster stars in NGC 1245 are considerably more spatially extended than the brighter stars. The fainter stars being spatially extended is almost certainly a consequence of the effects of mass segregation, which we expect to be important for a cluster of this mass and age. We provide additional evidence for mass segregation in § 5 and discuss the implications of this mass segregation more thoroughly in § 6.

The radial profile of NGC 1245 implies that the faint-cluster members may actually extend significantly beyond our field of view. The radial profile for the 1.3 m data predicts that, at 1σ , 40% to 100% of the faint ($V > 17.8$) stars outside $10'$ of the cluster center and within the field of view are cluster members. The strong cluster contribution in the outer periphery of our observed field hampers our ability to obtain an accurate statistical subtraction of the field star contamination necessary to determine the mass function for NGC 1245. We discuss this additional complication and our solution in § 5.

5. MASS FUNCTION

Typically an assumed mass-luminosity relation allows the transformation of the observed luminosity function to derive the present-day mass function (Chabrier 2003). In contrast, we assign a mass to each star individually using our best-fit isochrone. Minimizing a star’s individual χ_i^2 (eq. [2]) using the best-fit isochrone parameters determines the star’s mass. To determine the mass for each star, we use the high-quality 2.4 m photometry shown in the bottom panel CMDs of Figure 2, since it covers a much larger field of view. We reduce field star contamination of the cluster mass function by restricting the sample to stars with $\chi_i^2 < 0.04$. This χ_i^2 cutoff selects a region in the V , $(B-V)$ CMD roughly similar to the main-sequence selection used in the isochrone fit but naturally selects stars based on their proximity to the isochrone in all three passbands.

Despite the large field of view of the 2.4 m data, the radial profile of the cluster suggests that there exists a significant number of low-mass cluster members out to the limits of our field of view. Lacking observations of a field offset from the cluster, the Besançon theoretical galaxy model (Robin & Crézé 1986) provides an alternative method to correct the observed mass function for field star contamination. We obtain from the Besançon galaxy model electronic database the stellar properties and photometry for a 1 deg^2 field centered on the cluster’s galactic coordinates without observational errors. A spline fitted to the median photometric error in 0.5 mag bins in each passband allows us to simulate the observed errors in the theoretical galaxy field photometry. We add a zero-mean, unit standard-deviation Gaussian random deviate scaled to the observed photometric error model to the theoretical galaxy field photometry. We apply the same error-selection criteria ($\sigma < 0.08$) as was applied to the observed CMD and place a saturation cutoff at $V = 14.0$ mag to the theoretical CMD.

To make a qualitative comparison between the theoretical field CMD and the observed CMD, we adjust the theoretical

CMD for the smaller observed 2.4 m field of view. In the comparison, a star is included in the theoretical CMD only if a uniform random deviate is less than the ratio between the two field of views. Figure 7 compares the CMDs of the theoretical galaxy model in the top panels and the observations for stars beyond $12.7'$ of the cluster center for the 2.4 m data in the bottom panels. The dashed line shows the best-fit isochrone for reference. As shown in Figure 7, the theoretical and observed field CMDs are qualitatively very similar.

To calculate the field star contamination in the mass function, we first obtain the mass for the stars in the theoretical field CMD and apply the same $\chi_i^2 < 0.04$ selection in the same manner as the observed field CMD. For both the theoretical field CMD and observed cluster CMD, we calculate mass functions using even log-spaced intervals of $0.071 \log M_\odot$. Number counts from the entire 1 deg^2 field of view provide the basis for the theoretical galaxy mass function. The larger field of view of the theoretical galaxy model, as compared with the observed field, requires scaling of the number counts and corresponding Poisson error of the theoretical galaxy mass function by the ratio of fields of view. Subtracting the scaled theoretical galaxy field number counts from the observed number counts provides the cluster mass function. The cluster mass function is shown as the heavy solid line in the top panel of Figure 8. The top axis shows the median apparent V magnitude for the corresponding mass bin. The vertical dashed line delineates mass bins that are complete to better than 90%. Comparing the cluster mass function to a mass function calculated by subtracting the theoretical galaxy number counts without applying the photometric error selection criteria determines the completeness of a mass bin. The long-dashed line labeled “Salpeter” in Figure 8 illustrates the typical observed mass function slope, $\alpha = -1.35$. A power law in linear-mass, linear–number-count space fitted with weights to the mass function bins not affected by incompleteness yields a slope steeper than Salpeter, $\alpha = -3.12 \pm 0.27$.

To verify the validity of using the theoretical galaxy field in place of an observed off-cluster field, we calculate an alternative mass function using the observed field outside $12.7'$ of the cluster center for field contamination subtraction. The entire 2.4 m field of view again provides the basis for the observed number counts. The smaller field of view of the outer periphery requires scaling the field contamination number counts and corresponding Poisson error by the relative area factor, $f = 6.4$. The light solid line in the upper panel of Figure 8 shows the resulting cluster mass function using the outer periphery for determining the field contamination. The mass bin positions are offset slightly for clarity. The two mass functions agree within 1σ for all bins with $\log M > 0$ but disagree significantly at the low-mass end. The theoretical galaxy subtracted mass function contains greater number counts at the low-mass end, consistent with our conclusion that the outer regions of our observed field of view contain a significant number of low-mass cluster stars. Both mass functions contain a drop in the number counts at $\log(M) = 0.071$. We question the significance of this drop in the number counts. The drop occurs at a magnitude with some of the heaviest field star contamination, making the field star contamination subtraction less certain.

As further evidence of mass segregation in NGC 1245, we calculate the mass function inside and outside a radius of $4.2'$ from the cluster center. According to the cluster radial profile, this radius roughly separates half of the cluster members. The inner and outer mass functions are shown as the solid and

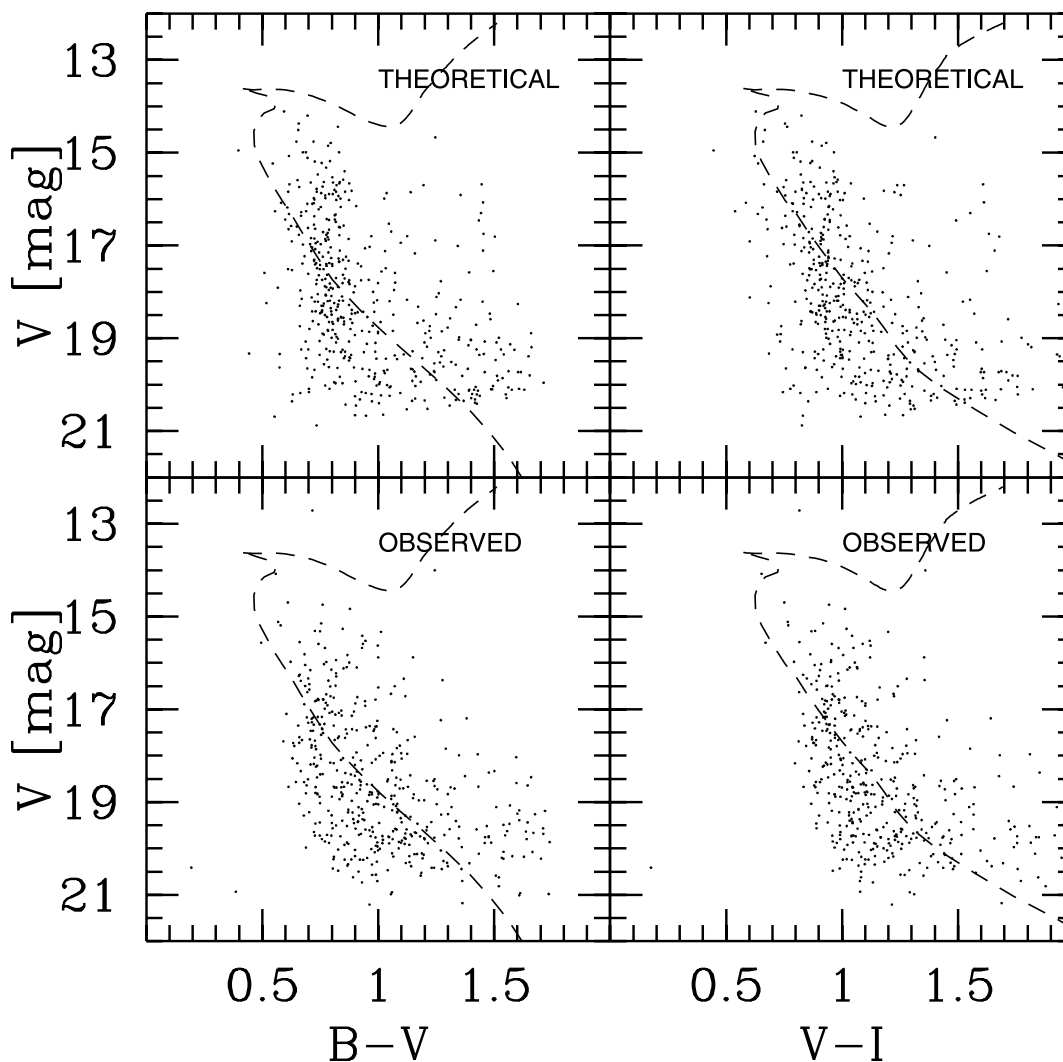


FIG. 7.—*Top*: Besançon theoretical galaxy model V , $(B-V)$ and V , $(V-I)$ CMDs for the Galaxy position of NGC 1245 (Robin & Cr ez e 1986). Photometric errors and selection criteria are included in the theoretical galaxy to match the observed CMDs shown in the bottom panels. *Bottom*: Observed V , $(B-V)$ and V , $(V-I)$ CMDs for stars beyond 12.7 of the cluster center using the 2.4 m data. In all panels, the dashed line shows the best-fit isochrone.

short-dashed lines, respectively, in the bottom panel of Figure 8. The fit to the inner region mass function yields a shallower slope that is consistent with Salpeter, $\alpha = -1.37 \pm 0.2$. Ignoring the highest mass bin, the best-fit slope for the inner region is even shallower, $\alpha = -0.56 \pm 0.28$. We find that the outer region is highly enriched in low-mass stars. The outer region mass function has a very steep slope, $\alpha = -7.1 \pm 1.2$. The mass bins with the down pointing arrows have negative values, and the point represents the 2σ upper confidence limit. Since the mass function is fitted in linear space, the fit includes bins with negative values.

The radial profile and mass function demonstrate that a significant fraction of the low-mass cluster members reside in the outer periphery of the cluster. Previous studies of NGC 1245 generally find Salpeter and shallower slopes for the mass function (Carraro & Patat 1994; Subramaniam 2003). As Subramaniam (2003) warned, the smaller fields of view of these previous studies, from which the field contamination is determined, bias the mass function against low-mass members that reside in the outer periphery of the cluster. The mass functions from the previous studies agree well with our mass function for the interior of NGC 1245, but we conclude that a

steeper slope than Salpeter, $\alpha = -3.12 \pm 0.27$, is more appropriate for NGC 1245 as a whole down to the completeness limit of $M = 0.8 M_{\odot}$.

Our deeper CMD, obtained from combining the MDM 2.4 m data (Fig. 3), allows us to extend the mass function to even lower masses. Determining the mass function to lower masses improves our mass estimate of the cluster, calculated in the following section. To calculate the mass function, we follow the same procedure as outlined above. At these fainter magnitudes, the theoretical galaxy field overpredicts the number of stars. Thus we must resort to using the outer periphery of the MDM 2.4 m field of view for estimating the field contamination. The heavy solid line in Figure 9 shows the resulting mass function based on the deeper CMD. The light solid line reproduces the equivalent mass function from Figure 8 based on the shallower CMD data. The vertical dashed line represents the completeness limit at $M = 0.56 M_{\odot}$. The deep mass function has a slope, $\alpha = -0.5 \pm 0.4$, significantly steeper than the slope for the shallow mass function $\alpha = -2.8 \pm 0.8$. The significantly differing slopes suggest there is a turnover in the mass function at $\log(M/M_{\odot}) = -0.05$. Fitting to the last three complete mass bins in the

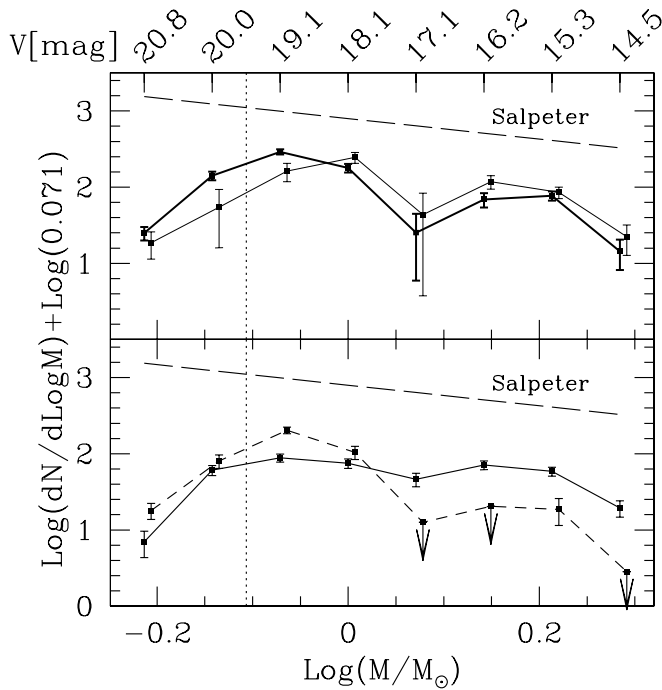


FIG. 8.—*Top*: Mass function using a theoretical galaxy model (*heavy solid line*) and outer periphery of the field of view (*light solid line*) for determining the field contamination. The vertical line delineates mass bins complete to better than 90%. *Bottom*: Mass function for stars inside (*solid line*) and outside (*dashed line*) 4.3. The down pointing arrows represent mass bins with negative values, and the point on the tail represents the 2σ upper limit.

deep mass function yields a slope $\alpha = 1.8 \pm 0.5$. The low-mass end of the deep mass function likely does not fall as steeply as measured, since we use the outer periphery of the MDM 2.4 m field of view to quantify the field contamination, which likely contains many low-mass cluster members. Thus, the measured slope at the low-mass end represents an upper limit.

6. TOTAL MASS AND DYNAMICS

Numerous dynamical processes take place in open clusters. Interactions between the cluster members dramatically affect binary and planetary systems, mass segregation within the cluster, and the timescale for cluster dissolution (Hurley & Shara 2002a, 2002b; Giersz & Heggie 1997; Portegies Zwart et al. 2001). The cluster's initial total mass sets the timescale for these dynamical processes and governs its dynamical evolution. Unfortunately, several difficulties prevent a completely empirical determination of the total mass of NGC 1245. First, as we show in § 4, the surface density profile suggests the cluster extends significantly beyond our field of view. Second, a substantial population of low-mass cluster members exists below the completeness limit of our mass function. Third, we do not resolve binary systems. Therefore, the total mass in *observed* cluster members ($\sim 820 M_\odot$) only places a lower limit on the current cluster mass. Finally, even overcoming the previously discussed difficulties, stellar evolution and evaporation result in additional complications for determining the initial birth mass of the cluster.

In order to provide a rough estimate of the current total cluster mass, we must adopt a number of assumptions in order to extrapolate the observed mass to the total mass. We must account for stars outside our survey area and stars fainter than our magnitude limit. The total cluster mass determined by

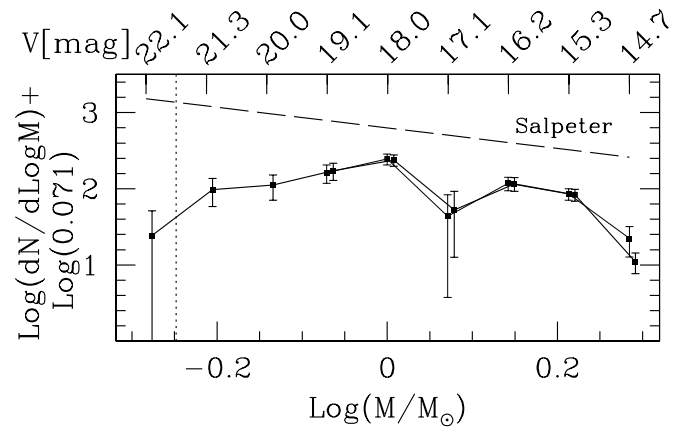


FIG. 9.—Heavy solid line shows the mass function calculated from the deep 2.4 m data (Fig. 3) using the outer periphery of the field of view for determining the field contamination. The vertical line delineates mass bins complete to better than 90%. The light solid line reproduces the equivalent mass function based on the shallow 2.4 m data as shown by the light solid line in the top panel of Fig. 8.

integrating the radial profile model we fitted in § 4 slowly converges and is unrealistically large for an integration to infinity. In reality, the tidal field of the Galaxy truncates the outer radius of the cluster. Therefore, we refitted the observed data set to the King profile (King 1962),

$$\Sigma = \Sigma_f + \Sigma_0 \left\{ \left[1 + \left(\frac{r}{r_c} \right) \right]^{-1/2} - \left[1 + \left(\frac{r_t}{r_c} \right) \right]^{-1/2} \right\}, \quad (5)$$

where r_t is the tidal radius of the cluster. Note that as $r_t \rightarrow \infty$ this profile reduces to the radial profile given in equation (4) for $\beta = 2$. For a given set of parameters, Σ_0 , r_c and r_t , the integral over equation (5) determines the total number of stars,

$$N = \pi r_c^2 \Sigma_0 \left\{ \frac{\ln(1+x_t) - [3(1+x_t)^{1/2} - 1][(1+x_t)^{1/2} - 1]}{1+x_t} \right\}, \quad (6)$$

where $x_t \equiv (r_t/r_c)^2$ (King 1962). The total mass is then $M = \langle m \rangle_{\text{obs}} N$, where $\langle m \rangle_{\text{obs}} = 1.00 M_\odot$ is the average mass of observed cluster stars.

Unfortunately, King profile fits to either data set yield only lower limits for the value of r_t . The lower limit only for r_t is primarily due to the covariance between r_t and Σ_f . Therefore, we need an additional constraint on either the surface density of field stars or the tidal radius in order to determine the total cluster mass. Attempting to constrain the fit using values of Σ_f determined from the theoretical galaxy field star counts (see § 5) results in unrealistically large values of $r_t > 40'$. Thus, we adopt a different approach.

The tidal radius of the cluster is set by both the local tidal field of the Galaxy and the total mass of the cluster. We can estimate the tidal radius as the radius of the Lagrange point (Binney & Tremaine 1987),

$$r_t = \left(\frac{M}{3M_{\text{MW}}} \right)^{1/3} D, \quad (7)$$

where D is the distance of the cluster from the center of the Galaxy, M is the total mass of the cluster, and M_{MW} is the mass of the Galaxy interior to D . For our derived distance of

$d = 2850$ pc, assuming $R_0 = 8$ kpc, and Galactic coordinates ($l = 147.6$, $b = -8.9$), the Galactocentric distance of NGC 1245 is $D = 10.50$ kpc. For a flat rotation curve with $v = 220$ km s $^{-1}$, we find $M_{\text{MW}} = 1.18 \times 10^{11} M_{\odot}$, and thus $r_t \simeq 20 \text{ pc} (M/2500 M_{\odot})^{1/3}$.

We use equations (6) and (7) to solve for the total cluster mass M and tidal radius r_t , while simultaneously constraining r_c , Σ_f , and Σ_0 from fitting equation (5) to the observed radial surface density profile. However, we must first account for low-mass stars that are below our detection limit. To do this, we use the best-fit mass function ($dN/d \log M \propto M^{\alpha}$, with $\alpha = -3.12$) to the turnover in the mass function at $0.85 M_{\odot}$. For stars between the hydrogen-burning limit and $0.85 M_{\odot}$, we assume $\alpha = 1.0$. Thus, our assumed cluster mass function is

$$\frac{dN}{d \log M} \propto \begin{cases} M^{-3.12}, & M > 0.85 M_{\odot}, \\ M^{1.0}, & 0.08 M_{\odot} < M < 0.85 M_{\odot}. \end{cases} \quad (8)$$

The adopted mass function slope at the low-mass end, $\alpha = 1.0$, is a compromise between our measured lower limit to the slope, $\alpha = 1.8$ (see § 5), and other clusters that have an observed mass function slope as shallow as $\alpha \sim 0.4$ at the low-mass end (Prisinzano et al. 2001; Bouvier et al. 2003). This yields a total cluster mass (in our field of view) of $\sim 1312 M_{\odot}$ and a correction factor of 1.61 to the observed mass in cluster stars.

We use an iterative procedure to determine M and r_t . We assume a value of r_t and then fit the King profile (eq. [5]) to the observed radial density profile. The best-fit King profile yields trial values of r_c , Σ_f , Σ_0 , and the total number of cluster stars via equation (6). We then apply the correction factor to account for stars below our completeness limit to determine the total cluster mass, $M = 1.61 \langle m \rangle_{\text{obs}} N$. We then use equation (7) to predict a new value for r_t . The procedure iterates until convergence with a tidal radius of $r_t \simeq 20'$ (16.5 pc) and a total mass of $M = 1312 \pm 90 M_{\odot}$, where the error is the 1σ statistical error from the fit. We determined the total cluster mass using the shallow 2.4 m data set as this is the data set used to determine the mass correction factor and surface density profile.

The mass correction factor, sensitive to the mass function slope at the low-mass end, dominates the uncertainty in the cluster mass. For example, varying the logarithmic slope of the mass function below $0.85 M_{\odot}$ in the range $0.6 \leq \alpha \leq 1.4$ changes the derived total mass by +200–140 M_{\odot} .

Our derived mass does not account for the presence of unresolved binaries. Without knowledge of the properties of the binary population, it is difficult to assess the magnitude of the correction. However, for a large binary fraction, the correction could be as large as 50%. We have also not attempted to correct the derived present-day mass for evolutionary effects, such as evaporation or stellar evolution, to derive an initial cluster mass. For our adopted mass function (eq. [8]), the correction to the total cluster mass due to stellar evolution is small, $\sim 12\%$. About 10% of the cluster stars are lost to the Galaxy per relaxation time (Spitzer 1987; Portegies Zwart et al. 2001). Since the current age of NGC 1245 is approximately 8 times larger than the current relaxation time (see below), it is possible that the cluster has lost an appreciable amount of mass over its lifetime. The numerical N -body simulations of Portegies Zwart et al. (2001) predict the initial cluster mass based on the current number of red giant stars. Using their equation (1), an age of 1 Gyr for NGC 1245 and a total of 40 observed red giant stars yields an initial total cluster mass, $M_0 = 3120 M_{\odot}$.

The relevant quantity that determines the timescale for dynamical evolution of a stellar cluster is the half-mass relaxation timescale (Spitzer 1987),

$$t_{\text{rlx}} = 0.138 \left(\frac{r_{\text{hm}}^3}{G \langle m \rangle} \right)^{1/2} \frac{N^{1/2}}{\ln \Lambda}. \quad (9)$$

Here r_{hm} is the radius enclosing half of the total mass of the cluster, $\langle m \rangle \simeq 0.63 M_{\odot}$ is the average mass of cluster members, and $\ln \Lambda \simeq \ln 0.4N$ is the Coulomb logarithm. This is roughly the average time over which the velocity of a typical cluster member changes by order unity due to random encounters with other cluster members. For NGC 1245, $r_{\text{hm}} = 3.8$ pc, and $t_{\text{rlx}} \simeq 130$ Myr. Since the age of NGC 1245 is ~ 1 Gyr, we expect this cluster to be dynamically quite evolved. Therefore, the evidence of mass segregation found in §§ 4 and 5 is not surprising.

7. CONCLUSION

In this paper, we report our results based on BVI photometry of the open cluster NGC 1245 using the MDM 1.3 m and 2.4 m telescopes. Here we improve on the observations for this cluster by covering a 6 times greater area, obtaining the first CCD I -band photometric data, and acquiring the first CCD data under photometric conditions. With these significant improvements over earlier studies, we are able to determine more precisely the physical parameters of the cluster as a whole, rather than just the inner cluster core. Our photometric data resolve some of the confusion in the literature regarding the correct photometric zero point for this cluster (Wee & Lee 1996; Subramaniam 2003). Based on isochrone fits employing the Y^2 calculations (Yi et al. 2001), we confirm the findings of Wee & Lee (1996) and (Marshall et al. 2004) that this cluster has a slightly subsolar metallicity, $[\text{Fe}/\text{H}] = -0.05 \pm 0.03$ (statistical) ± 0.08 (systematic). Our best-fit age is $1.04 \pm 0.02 \pm 0.09$ Gyr. In contrast to previous studies, we do not find evidence of significant differential reddening. We find a V -band extinction of $A_V = 0.68 \pm 0.02 \pm 0.09$, and with the aid of 2MASS K_s photometry, we constrain the ratio of absolute-to-selective extinction to be $R_V = 3.2 \pm 0.2$. The resulting absolute distance modulus is $(m - M)_0 = 12.27 \pm 0.02 \pm 0.12$.

With the large field of view provided by the MDM 8K Mosaic imager, we find NGC 1245 is a highly relaxed cluster; a majority of the low-mass cluster members reside in an extended halo. The mass function slope, $\alpha = -3.12 \pm 0.27$, down to $M = 0.85 M_{\odot}$ is steeper than the Salpeter value of $\alpha = -1.35$, found by earlier studies. The previous studies did not have a sufficient field of view to detect the low-mass cluster members that preferentially reside in the outer periphery of the cluster. Based on the observed stellar surface density profile and an extrapolated mass function, we derive a total cluster mass, $M = 1300 \pm 90 \pm 170 M_{\odot}$.

This paper is the first in a series for the Search for Transiting Extrasolar Planets in Stellar Systems (STEPSS) project. The main goal of the STEPSS project is to determine the fraction of stars with close-in, Jupiter-sized planets using the photometric transit technique. By searching for extrasolar planets in open clusters of known metallicity, stellar density, and age, we hope to constrain the impact of these parameters on the resulting planetary systems. The accurate physical parameters for NGC 1245 derived in this paper will be used in the analysis of the 19 night run targeting NGC 1245 to search

for transiting extrasolar planets (Gaudi et al. 2004). The NGC 1245 transit search, consisting of 5 minute time resolution *I*-band photometry taken over 19 nights, will also provide valuable information on the variable star content of NGC 1245 (Pepper et al. 2004).

This publication makes use of data products from the Two Micron All Sky Survey, which is a joint project of the Uni-

versity of Massachusetts and the Infrared Processing and Analysis Center, California Institute of Technology, funded by the National Aeronautics and Space Administration and the National Science Foundation. This work was supported in part by NASA through a Hubble Fellowship grant from the Space Telescope Science Institute, which is operated by the Association of Universities for Research in Astronomy, Inc., under NASA contract NAS 5-26555, the Menzel Fellowship from the Harvard College Observatory, and by NASA grant NAG 5-13129.

REFERENCES

- Adams, F. C., & Myers, P. C. 2001, *ApJ*, 553, 744
 Bessell, M. S., & Brett, J. M. 1988, *PASP*, 100, 1134
 Binney, J., & Tremaine, S. 1987, *Galactic Dynamics* (Princeton: Princeton Univ. Press)
 Bouvier, J., Moraux, E., Stauffer, J. R., Barrado y Navascués, D., Cuillandre, J.-C. 2003, in *IAU Symp. 211, Brown Dwarfs*, ed. E. Martin (San Francisco: ASP), 147
 Burke, C. J., DePoy, D. L., Gaudi, B. S., Marshall, J. L., & Pogge, R. W. 2003, in *ASP Conf. Ser. 294, Scientific Frontiers in Research on Extrasolar Planets*, ed. D. Deming & S. Seager (San Francisco: ASP), 379
 Cardelli, J. A., Clayton, G. C., & Mathis, J. S. 1989, *ApJ*, 345, 245
 Carraro, G., & Patat, F. 1994, *A&A*, 289, 397
 Chabrier, G. 2003, *PASP*, 115, 763
 Crotts, A. P. S. 2001, *BAAS*, 33, 792
 Cutri, R. M., et al. 2003, *Explanatory Supplement to the 2MASS All Sky Data Release* (Pasadena: Caltech)
 de Bruijne, J. H. J., Hoogerwerf, R., & de Zeeuw, P. T. 2001, *A&A*, 367, 111
 Friel, E. D. 1995, *ARA&A*, 33, 381
 Gaudi, B. S., Burke, C. J., DePoy, D. L., Pogge, R. W. 2004, in preparation
 Giersz, M., & Heggie, D. C. 1997, *MNRAS*, 286, 709
 Girardi, L., Bressan, A., Bertelli, G., & Chiosi, C. 2000, *A&AS*, 141, 371
 Gould, A., Stutz, A., & Frogel, J. A. 2001, *ApJ*, 547, 590
 Grocholski, A. J., & Sarajedini, A. 2003, *MNRAS*, 345, 1015
 Hoag, A. A., Johnson, H. L., Iriarte, B., Mitchell, R. I., Hallam, K. L., & Sharpless, S. 1961, *Publ. US Naval Obs.*, 17, 347
 Hurley, J. R. & Shara, M. M. 2002a, *ApJ*, 565, 1251
 ———. 2002b, *ApJ*, 570, 184
 Janes, K. A., Tilley, C., & Lyngå, G. 1988, *AJ*, 95, 771
 Jennens, P. A., & Helfer, H. L. 1975, *MNRAS*, 172, 681
 King, I. 1962, *AJ*, 67, 471
 Landolt, A. U. 1992, *AJ*, 104, 340
 Lejeune, T., Cuisinier, F., & Buser, R. 1998, *A&AS*, 130, 65
 Lyngå, G. 1987, *Catalogue of Open Cluster Data* (5th ed.; Lund: Lund Obs.)
 Marshall, J. L., DePoy, D. L. & Burke, C. J. 2004, in preparation
 Mighell, K. J., Sarajedini, A., & French, R. S. 1998, *AJ*, 116, 2395
 Nilakshi, Sagar, R., Pandey, A. K., & Mohan, V. 2002, *A&A*, 383, 153
 Paulson, D. B., Sneden, C., & Cochran, W. D. 2003, *AJ*, 125, 3185
 Pepper, J., Burke, C. J., Gaudi, B. S., DePoy, D. L. & Pogge, R. W. 2004, in preparation
 Perryman, M. A. C., et al. 1998, *A&A*, 331, 81
 Pinsonneault, M. H., Terndrup, D. M., Hanson, R. B., & Stauffer, J. R. 2003, *ApJ*, 598, 588
 Portegies Zwart, S. F., McMillan, S. L. W., Hut, P., & Makino, J. 2001, *MNRAS*, 321, 199
 Press, W. H., Teukolsky, S. A., Vetterling, W. T., & Flannery, B. P. 2001, *Numerical Recipes* (Cambridge: Cambridge Univ. Press)
 Prisinzano, L., Carraro, G., Piotto, G., Seleznev, A. F., Stetson, P. B., & Saviane, I. 2001, *A&A*, 369, 851
 Robin, A., & Crézé, M. 1986, *A&A*, 157, 71
 Spitzer, L. 1987, *Dynamical Evolution of Globular Clusters* (Princeton: Princeton Univ. Press)
 Stetson, P. B. 1987, *PASP*, 99, 191
 Stetson, P. B., et al. 1998, *ApJ*, 508, 491
 Subramaniam, A. 2003, *Bull. Astron. Soc. India*, 31, 49
 Wee, S.-O., & Lee, M. G. 1996, *J. Korean Astron. Soc.*, 29, 181
 Yi, S., Demarque, P., Kim, Y.-C., Lee, Y.-W., Ree, C. H., Lejeune, T., & Barnes, S. 2001, *ApJS*, 136, 417